Smart Materials in Manufacturing 3 (2025) 100093

Contents lists available at ScienceDirect

Smart Materials in Manufacturing

journal homepage: www.keaipublishing.com/en/journals/smart-materials-in-manufacturing

Research Paper

High-temperature oxidation behavior of SLM-processed and forged GH5188 Co-based superalloy

Chao Yang [a,1], Xue Chen [b,1], Yusheng Tian [c], Yifeng Tang [c], Shiping Cai [c], Wei Wei [e,*], Qianli Huang [f,**], Hang Guo [d], Aihui Huang [c,***], Paul K. Chu [g]

[a] National Engineering Research Center of Light Alloy Net Forming, Shanghai Jiao Tong University, Dongchuan Road No. 800, Shanghai, 200240, China
[b] School of Aeronautics and Astronautics, Sichuan University, Chuanda Road, Shuangliu District, Chengdu, 610065, China
[c] Suzhou Laboratory, Ruoshui Road, Suzhou Industrial Park, No. 388, Suzhou, 215000, China
[d] Yan'an Yanhong Intelligent Manufacturing Technology Development Co., Ltd., Zaoyuan, Baota District, Yan'an, Shaanxi, 716000, China
[e] Yan'an Vocational and Technical College, Zaoyuan, Baota District, Yan'an, 716000, China
[f] State Key Laboratory of Powder Metallurgy, Central South University, Lushan South Road, No. 932, Changsha, 410083, China
[g] Department of Physics, Department of Materials Science & Engineering, and Department of Biomedical Engineering, City University of Hong Kong, Tat Chee Avenue, Kowloon, Hong Kong, 999077, China

ARTICLE INFO

Keywords:
Co-based superalloy
Selective laser melting
High-temperature oxidation
Oxidation resistance
Microstructure refinement

ABSTRACT

The high-temperature oxidation behavior of GH5188 cobalt-based superalloy, fabricated via selective laser melting (SLM) and forging, is investigated to elucidate the impact of additive manufacturing on oxidation resistance. SLM-processed samples exhibit a hierarchical microstructure with nanoscale carbides (~80 nm) pinned at cellular boundaries (100 nm to micrometer scale), contrasting with the equiaxed grains (~10 μm) and coarse W-rich M_6C carbides (~5 μm) in forged samples. After isothermal oxidation at 1000 °C and 1100 °C for 200 h, SLM samples show significantly lower mass gains compared to forged samples (69 % and 75 % of forged values), attributed to enhanced oxide scale adhesion and stability. Cyclic oxidation at 1000 °C for 50 cycles reveals stable mass gains in SLM samples (37 % of forged value) with minimal cracking, while forged samples suffer severe spallation due to volatile WO_3 formation from coarse carbides. This study demonstrates that SLM's refined microstructure suppresses deleterious carbide decomposition, offering a novel strategy to enhance the oxidation resistance of Co-based superalloys for aerospace and high-temperature applications.

1. Introduction

Solid solution strengthened Co-based superalloys are widely used in high-temperature applications due to their favorable properties, such as high temperature tolerance up to 1100 °C, thermal conductivity, and resistance to hot corrosion and oxidation [1–3]. Unlike Ni-based superalloys, which show negative lattice misfits, the positive lattice misfit of Co-based superalloys results in distinct physical and mechanical characteristics [4]. The GH5188 alloy (Haynes-188), a representative Co-based superalloy boasting a small thermal expansion coefficient and superior oxidation resistance, is used in combustor chambers, transition ducts, afterburners, and liquid oxygen posts in space shuttle engines [5–7]. However, prolonged exposure to high-temperature oxidizing atmospheres leads to oxide scale spallation and degradation, consequently compromising the service life and corrosion protection [8]. Hence, a good understanding of the oxidation behavior of these superalloys is crucial to performance optimization under extreme conditions.

The high-temperature oxidation resistance of superalloys depends on the formation and stability of the protective oxide layer, such as Cr_2O_3 and Al_2O_3, which can vary significantly for different alloy compositions

Peer review under the responsibility of Editorial Board of Smart Materials in Manufacturing
* Corresponding author.
** Corresponding author.
*** Corresponding author.
E-mail addresses: chaoyang0315@163.com (C. Yang), chenxuescu@163.com (X. Chen), tianys@szlab.ac.cn (Y. Tian), tangyf@szlab.ac.cn (Y. Tang), caisp@szlab.ac.cn (S. Cai), double_w@foxmail.com (W. Wei), hql1990@163.com (Q. Huang), 15091721302@163.com (H. Guo), huangah@szlab.ac.cn (A. Huang), paul.chu@cityu.edu.hk (P.K. Chu).
[1] These authors contributed equally to this work.

https://doi.org/10.1016/j.smmf.2025.100093
Received 10 May 2025; Received in revised form 3 August 2025; Accepted 19 August 2025
Available online 13 September 2025

and environmental conditions [9,10]. Previous studies on cobalt-based superalloys have demonstrated the role of alloying elements in oxide formation and stability. Researchers have investigated the oxidation behavior of the Co-Cr-W superalloy and observed that moderate Cr promotes the formation of protective Cr_2O_3 scales, while W inhibits cation diffusion and oxide growth [11,12]. However, Co-based superalloys produced by casting or forging methods (CM) fail to meet modern industrial demands for intricate geometries, rapid production cycles, and cost efficiency [13,14].

Selective laser melting (SLM), an additive manufacturing (AM) technique, enables the fabrication of near-net-shape components with complex designs that are unattainable using conventional methods [15,16]. SLM has been successfully applied to various superalloys [17–22], including IN718, Hastelloy X, CM247LC, IN738, Rene 41, and GH5188. Recent studies on SLM-fabricated Ni-based superalloys, particularly Inconel 718 and Inconel 625, reveal distinct oxidation behaviors compared to conventionally manufactured (CM) counterparts, including: (1) no effect of microstructural anisotropy on oxidation properties, (2) slightly higher oxidation rates in AM materials [23–26]. Additionally, the heat treatment and surface modification can further optimize oxidation resistance of SLM-fabricated Ni-based superalloys [27]. However, research on oxidation behavior of SLM-processed Co-based superalloys, particularly GH5188, remains limited, with most studies focusing on mechanical properties rather than oxidation behavior [28,29]. The unique hierarchical microstructures induced by SLM, such as nanoscale carbides and cellular grains, have not been systematically explored for their impact on high-temperature oxidation resistance in Co-based superalloys with higher Cr content (~23 wt%) like GH5188, which may differ significantly from Ni-based superalloys due to compositional and microstructural variations. The unique hierarchical microstructures induced by SLM, such as nanoscale carbides and cellular grains, have not been systematically explored for their impact on high-temperature oxidation resistance in GH5188, which may differ significantly from Ni-based superalloys due to compositional and microstructural variations.

This study addresses this gap by comparing the oxidation behavior of SLM-fabricated and forged GH5188 superalloys under isothermal (900 °C, 1000 °C, 1100 °C) and cyclic (1000 °C) conditions. The microstructure, oxide scale morphology and oxidation kinetics of both variants are systematically analyzed to elucidate the oxidation mechanism. The new knowledge provides insights into the design and development of oxidation-resistant and SLM-fabricated Co-based superalloys for advanced high-temperature applications.

2. Materials and methods

2.1. Material preparation

The GH5188 cobalt-based superalloy powder was produced from a commercial GH5188 rod by gas atomization. The nominal composition of the alloy was 37.16 wt% Co, 23.38 wt% Ni, 23.07 wt% Cr, 14.10 wt% W, 1.24 wt% Fe, 0.91 wt% Mn, 0.08 wt% C, 0.4 wt% Si, and 0.06 wt% La. The powder had a spherical morphology, and laser diffraction shows the following particle parameters: $d_{10} = 19$ μm, $d_{50} = 33$ μm, and $d_{90} = 55$ μm in conjunction with a loose bulk density of 4.9 g/cm^3.

SLM was performed on the SLM 280HL system (SLM Solutions GmbH) equipped with a 300 W ytterbium fiber laser. A 3D model was designed in SolidWorks, exported in the STL format, and imported into the SLM printer software. The platform, consisting of the GH5188 superalloy to ensure compatibility, was preheated to 100 °C, and the chamber was purged with argon until the oxygen concentration was below 1000 ppm. Printing was conducted with a laser power of 300 W, at a scanning rate of 950 mm/s to produce a layer thickness of 40 μm. A bidirectional (alternating linear) scanning strategy was employed, with a 67° rotation between consecutive layers to minimize anisotropy in the X-Y plane [30–32]. Post-processing involved annealing of the SLM-fabricated GH5188 samples (hereafter "SLM") at 1180 °C for 40 min under argon according to the Q/5B 4022-1992 standard in order to relieve the residual stress and standardize the microstructure. For comparison, forged GH5188 samples (designated as "forged") with the same composition were prepared from the same commercial rod supplied by same manufacturer. These samples were also annealed at 1180 °C for 40 min to minimize processing-induced variations and ensure that the differences in the subsequent tests reflect the effects of the production method rather than the compositional or thermal history disparities.

2.2. Microstructural characterization

The microstructure of both the SLM-fabricated GH5188 and forged-GH5188 samples was examined on a scanning electron microscope (SEM, SUPERSCAN SSX-550, Shimadzu, Japan) and transmission electron microscope (TEM, Tecnai G2 F20 S-TWIN, FEI) equipped with energy-dispersive spectroscopy (EDS) for compositional analysis. The phases were determined by X-ray diffraction (XRD; Bruker D8 Advance) using Co K_α radiation ($\lambda = 1.7889$ Å) for a 2θ range of 20°–90° with a step size of 0.02°.

Prior to optical microscopy (OM; Zeiss Axio Observer) and SEM, the samples were sectioned, mounted, ground with SiC papers (up to 2000 grit), and polished with diamond suspensions (3 μm and 1 μm). Electrolytic etching was then carried out in aqua regia (3:1 HNO_3: HCl) at 2 V for 2 s to reveal the microstructural features. The TEM specimens were prepared using a conventional thinning protocol, which involved grinding with SiC papers (up to 4000 grit), polishing with diamond pastes (3 μm–0.25 μm), and dimpling using a Gatan Dimple Grinder (Model 656). Final thinning to electron transparency was achieved on a precision ion polishing system (PIPS 691, Gatan) using 5 kV argon ion sputtering and an incidence angle of 4°–6°. It should be noted that all the cross-sectional images were taken perpendicular to the building direction unless otherwise noted.

2.3. Isothermal oxidation

High-temperature oxidation tests were conducted on GH5188 samples fabricated by SLM and conventional forging (forged). Both types of samples were in the form of sheets with dimensions of 20 mm × 20 mm × 2 mm. The SLM samples were directly fabricated into sheet form without further machining, with the sheet plane parallel to the build platform and perpendicular to the laser scanning direction. The samples were ground with SiC papers (up to 2000 grit), polished with diamond suspensions (3 μm–1 μm), ultrasonically cleaned in an aqueous ethanol solution, and dried in a desiccator for 6 h. Initial mass measurements were performed on an electronic analytical balance (Sartorius CPA225D) with an accuracy of 0.1 mg, and five readings were averaged for each sample.

Isothermal oxidation was carried out in a muffle furnace at 900 °C, 1000 °C, and 1100 °C in static air. The samples were placed in pretreated alumina crucibles, which had been cleaned, dried, and preheated to 1150 °C for 15 h to remove contaminants to ensure thermal stability. The mass changes were recorded after 1, 2.5, 5, 7.5, 10, 12.5, 15, 25, 50, 75, 100, 150, and 200 h after the samples were removed from the furnace, cooled to room temperature in a desiccator. To improve the statistics, three parallel samples were tested under each condition (SLM and forging at each temperature) to generate the average mass gain.

2.4. Cyclic oxidation

Cyclic oxidation was performed on the SLM and forged samples (20 mm × 20 mm × 2 mm sheets), and the surface preparation and initial mass measurements were the same as those described in Section 2.3. Each cycle consisted of oxidation for 2 h at 1000 °C in static air and air cooling for 10 min at room temperature. The test was conducted in the

same box furnace using pre-treated alumina crucibles, similar to the isothermal setup. The mass gains were measured every 5 cycles (i.e., at 5, 10, 15, 20 cycles, etc.) for a total of 50 cycles, which corresponded to cumulative oxidation for 100 h. The samples were cooled in a desiccator after each measurement and weighed using the Sartorius CPA225D balance (accuracy ±0.1 mg). Three parallel samples were assessed under each condition, and the experimental parameters were the same as those in the isothermal oxidation test.

3. Results

3.1. Microstructure of SLM and forged GH5188 superalloys

The microstructures of the SLM and forged GH5188 samples were investigated by SEM, TEM, and XRD (Figs. 1–3). Fig. 1a–b shows a hierarchical microstructure in the SLM samples, comprising columnar substructures (~1 μm wide and hundreds of microns long) and cellular substructures (100–500 nm in diameter). The morphology resembling dendrites without secondary arms is formed by solute redistribution during rapid solidification in SLM, which induces constitutional undercooling and unique grain growth patterns distinct from conventional processing [33,34]. It should be noted that the SLM-fabricated GH5188 alloy exhibits a strong <001> fiber texture along the laser scanning direction according to our previous study [22]. Fig. 1c–d further disclose the cellular structures ranging from 500 nm to 1 μm in size and nanoscale precipitates (<100 nm) predominantly at cell boundaries. Fig. 1e–f disclose W and Cr enrichment in the precipitate (W: 41.05 wt%, Cr: 28.54 wt%) compared to the matrix (W: 12.36 wt%, Cr: 20.13 wt%) for the formation of W-rich carbide.

In contrast, the forged sample shows equiaxed grains approximately 10 μm in size without obvious texture and blocky precipitates (<5 μm) in the matrix (Fig. 2a–d). There are some finer precipitates at the grain boundaries, similar to the morphology of the large precipitates. EDS (Fig. 2e–f) shows that these precipitates are W-rich carbide. XRD

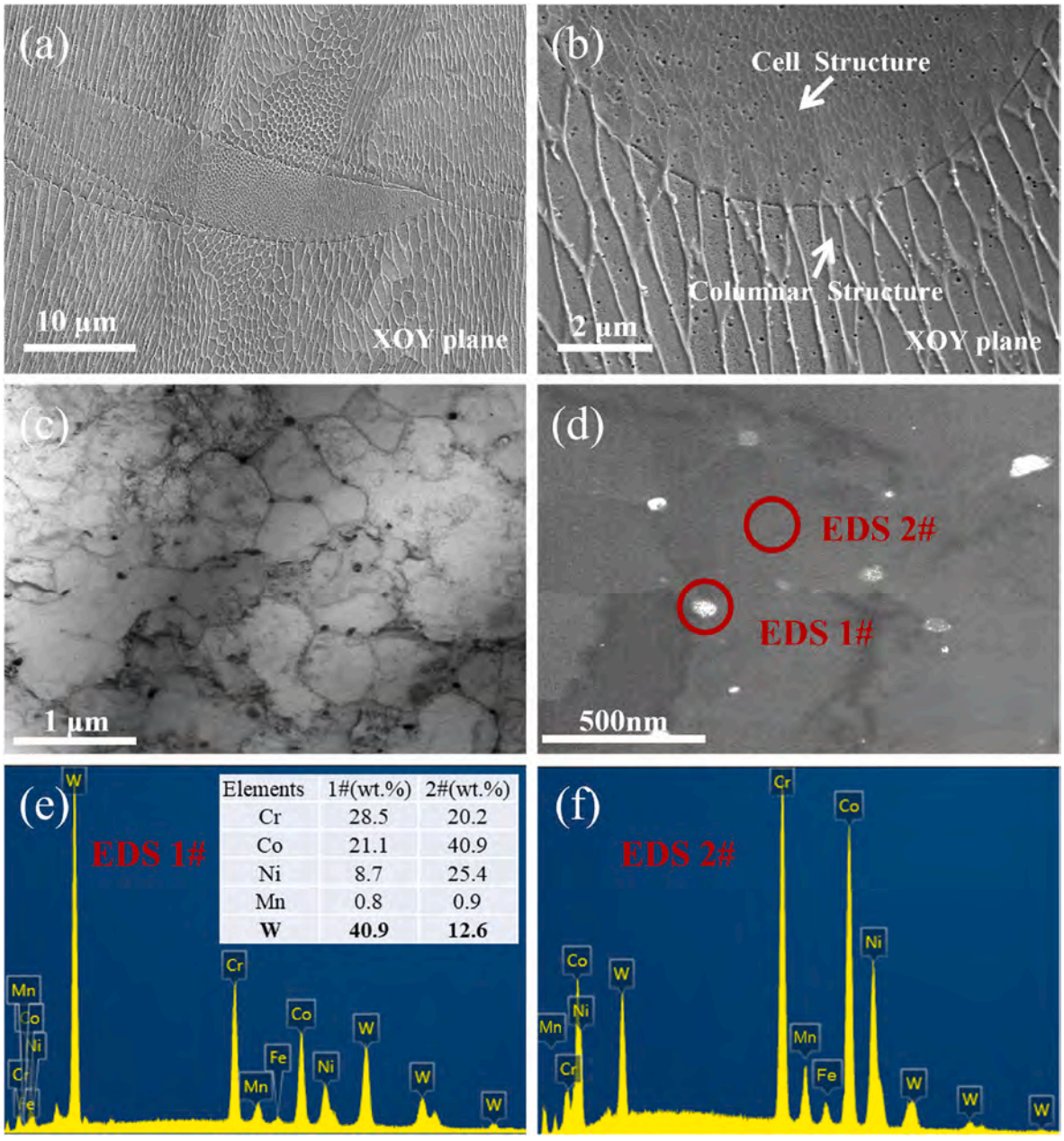

Fig. 1. Microstructural analysis of the SLM GH5188 superalloy: (a–b) Low and high-magnification SE images showing the overview of microstructure; (c–d) Low and high-magnification TEM-DF images revealing nanoscale precipitates; (e–f) EDS spectra acquired from regions 1 and 2 in (d).

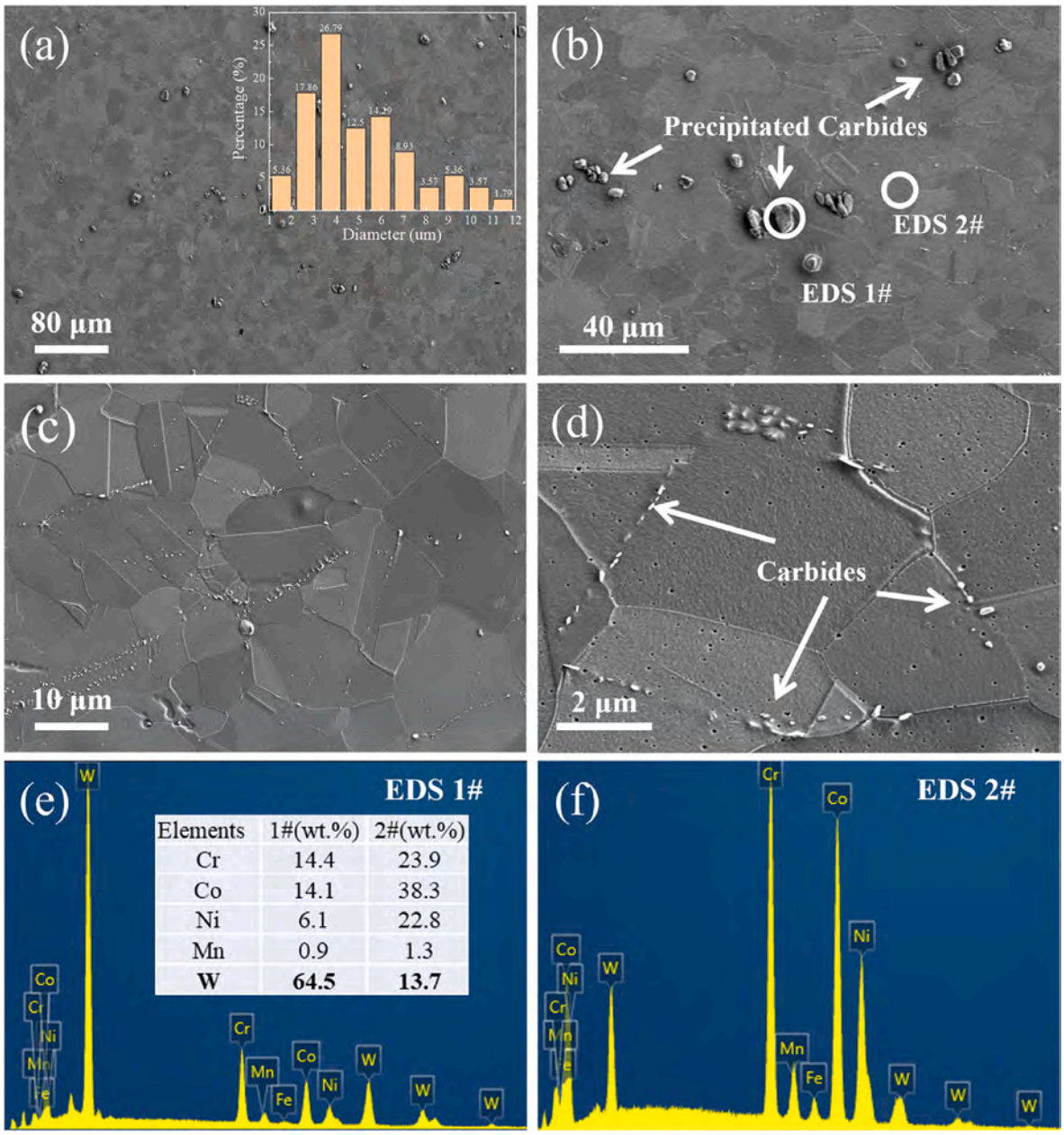

Elements	1#(wt.%)	2#(wt.%)
Cr	14.4	23.9
Co	14.1	38.3
Ni	6.1	22.8
Mn	0.9	1.3
W	**64.5**	**13.7**

Fig. 2. Microstructural analysis of the forged GH5188 superalloy: (a–d) Low and high-magnification SE images showing the microstructure of the forged sample; (e–f) EDS spectrum of the regions marked 1 and 2 in (b).

analysis (Fig. 3a) shows that the SLM sample consists of a single-phase FCC matrix, with no detectable carbide peaks. This is likely due to the nanoscale size and low volume fraction of the carbides, causing their diffraction signals to fall below the detection limit of conventional XRD. Conversely, the forged sample (Fig. 3b) displays peaks corresponding to both the FCC phase matrix and M_6C carbide, corroborating the W-rich precipitates observed by SEM and EDS. The larger carbide size in the forged stems results from the smaller cooling rate and wider dendrite spacing in solidification, which produces enrichment and carbide growth [32,35]. Therefore, it can be inferred that SLM refines the microstructure without altering the intrinsic FCC phase of GH5188, thereby distinguishing it from the coarser and W-rich carbide in the forged sample.

3.2. Isothermal oxidation at 900 °C, 1000 °C and 1100 °C

Fig. 4 presents the mass change of the SLM and forged-GH5188 superalloys after isothermal oxidation at 900 °C, 1000 °C and 1100 °C for 200 h. Both samples exhibit a consistent mass gain trend, with increases proportional to the oxidation temperature and duration. The SLM group shows superior oxidation resistance, with mass gains at 900 °C, 1000 °C, and 1100 °C being lower than those of the forged samples (Fig. 4a–b). Meanwhile, the mass gain curves for both variants follow an approximate parabolic relationship for different temperatures, indicative of diffusion-controlled oxidation kinetics. The oxidation rate can be described by the parabolic rate law shown in Eq. (1) [36]:

$$\left(\frac{\Delta m}{A}\right)^2 = k_p t + C, \tag{1}$$

where $\left(\frac{\Delta m}{A}\right)$ is the mass gain per unit area, k_p is the parabolic rate constant ($mg^2/(cm^4 \cdot h)$), t is the oxidation time, and C is the constant. According to the parabolic fits in Fig. 4c–d and Eq. (1), the parabolic rate constants of the SLM group are 9.64×10^{-4}, 2.07×10^{-3} and $1.09 \times$

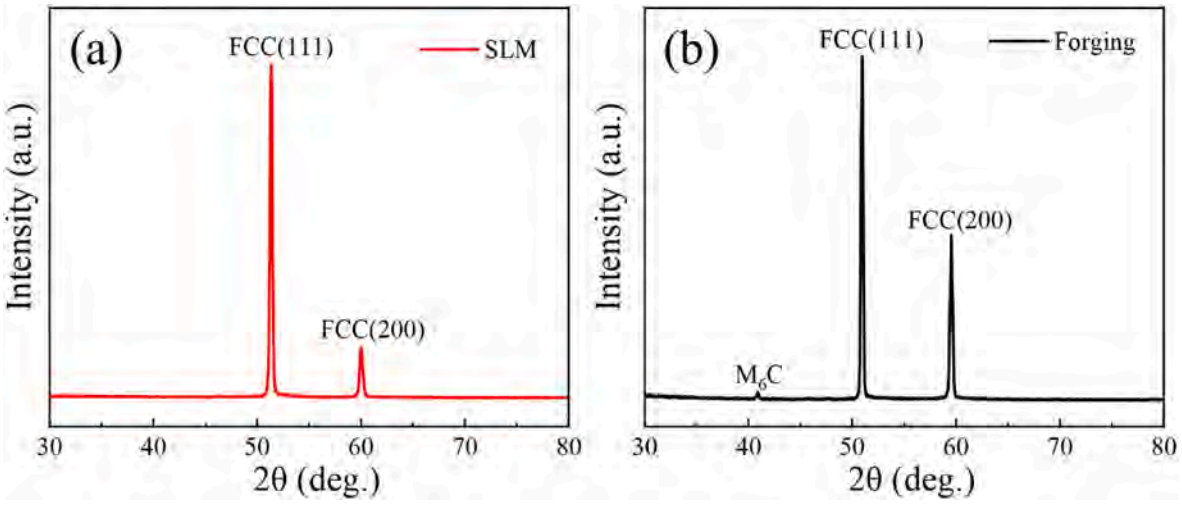

Fig. 3. XRD patterns of (a) SLM-GH5188 and (b) Forged GH5188 superalloys.

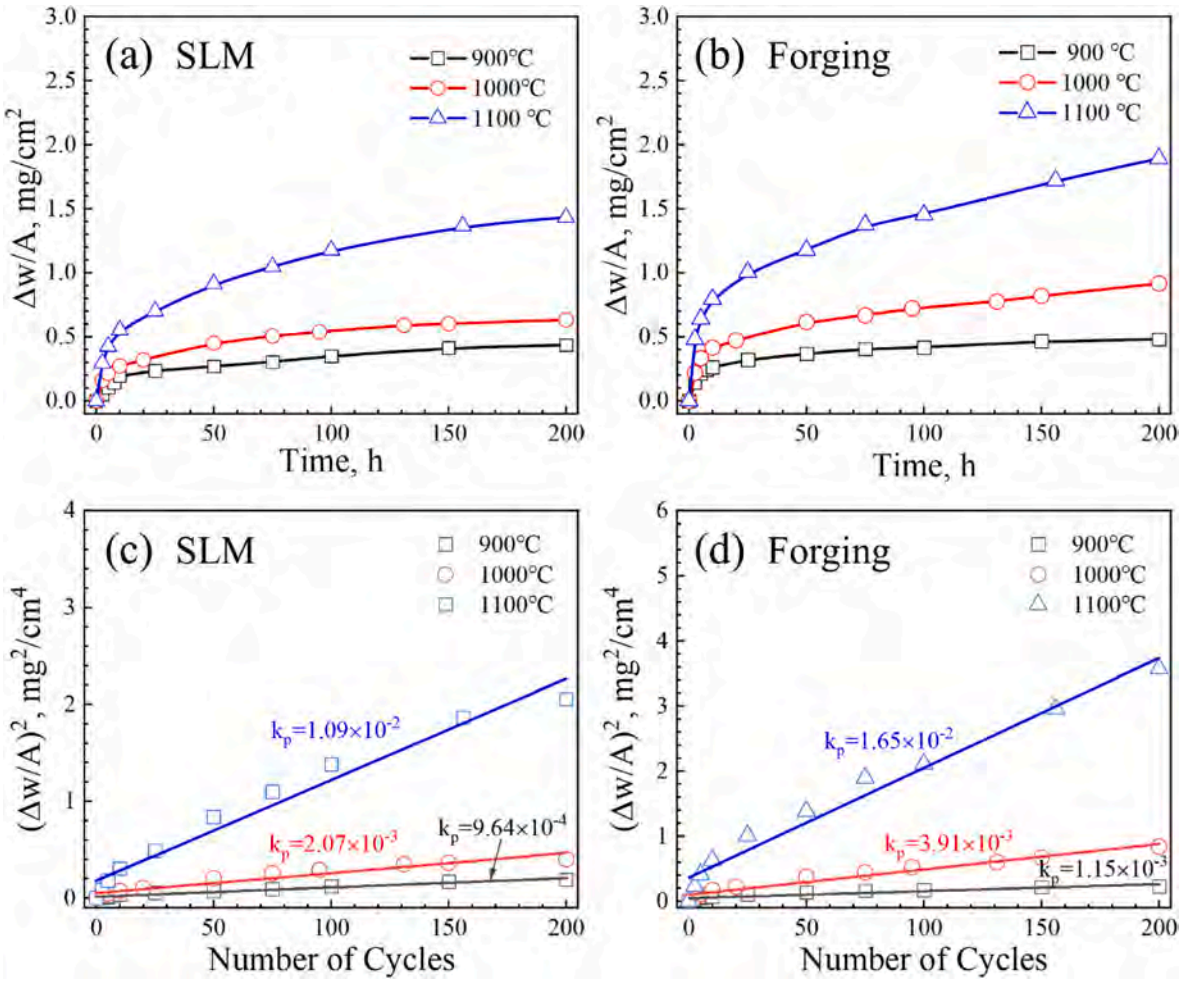

Fig. 4. Mass gains of the SLM and forged GH5188 superalloys after isothermal oxidation at 900 °C, 1000 °C, and 1100 °C for 200 h: (a–b) Parabolic mass gain curves; (c–d) Parabolic fits of $\left(\frac{\Delta m}{A}\right)^2$ versus time.

10^{-2} $mg^2/(cm^4h)$ at 900 °C, 1000 °C and 1100 °C, respectively, while the k_p values of the forged samples are 1.15×10^{-3}, 3.91×10^{-3} and 1.65×10^{-2} $mg^2/(cm^4h)$ at 900 °C, 1000 °C and 1100 °C, respectively. It translates into reductions of 16.2 %, 47.1 % and 34.1 % for the SLM samples compared to forged samples at the respective temperatures. The consistently smaller k_p values of the SLM samples confirm that GH5188 prepared by SLM has superior high-temperature oxidation resistance under different conditions.

Fig. 5 depicts the surface morphology of the SLM and forged samples after oxidation for 10 h at 900 °C, 1000 °C, and 1100 °C. A duration of

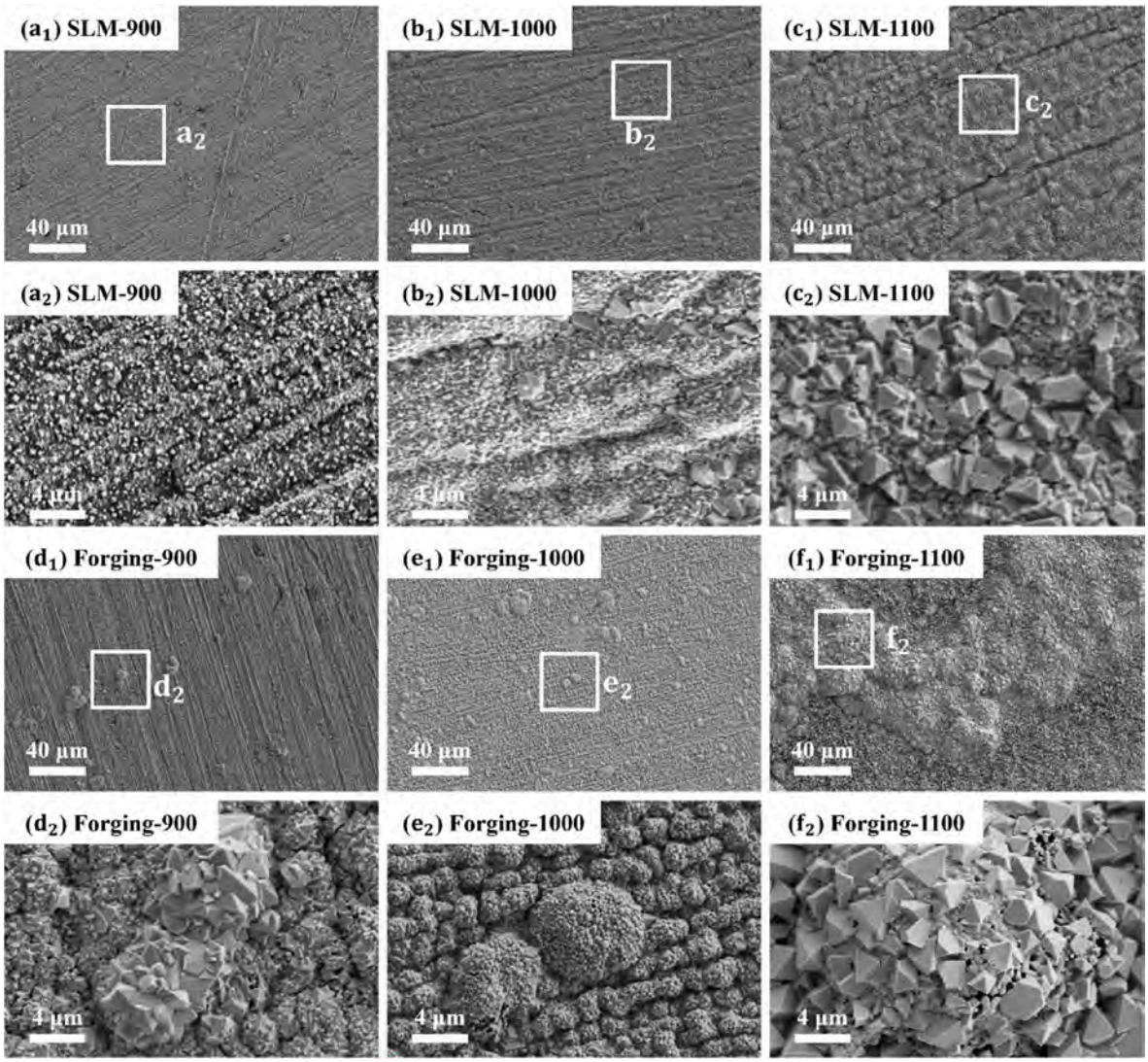

Fig. 5. Surface morphology of the SLM and forged samples after oxidation for 10 h at 900 °C, 1000 °C, and 1100 °C: (a_1-a_2, d_1-d_2) Low and high-magnification SE images after oxidation for 10 h at 900 °C; (b_1-b_2, e_1-e_2) Low and high-magnification SE images after oxidation for 10 h at 1000 °C; (c_1-c_2, f_1-f_2) Low and high-magnification SE images after oxidation for 10 h at 1100 °C.

10 h is selected to monitor early oxide development, as prolonged exposure risks oxide scale failure through thickening, cracking, as well as volatilization. At 900 °C, the oxide layers on both samples are thin, and grinding scratches are still visible (Fig. 5a_1, d_1). The forged sample exhibits spinel nodules (~5 μm) in a tumor-like structure on the oxidized surface (Fig. 5d_2), while the SLM sample shows a finer and uniformly distributed spinel structure (~100 nm) (Fig. 5a_2). After oxidation at 1000 °C, the surface morphology of the SLM sample shows the original scratches with larger spinel sizes and good distribution (Fig. 5b_1-b_2). In contrast, the forged sample exhibits a larger tumor-like structure and partial cavities, indicating the degradation of oxide scale during early oxidation (Fig. 5e_1-e_2). At 1100 °C, the SLM sample shows localized folding without the formation of tumor-like oxide and spinel size approaching the micrometer scale (Fig. 5c_1-c_2). The forged sample also displays inhomogeneous thickening and the lack of a tumor-like oxide structure. However, the loose and large spinel structure is found on the oxidized surface, and the cracks and internal cavities suggest oxide scale failure (Fig. 5f_1-f_2). Overall, both samples develop globular and spinel oxide structures after oxidation, but the SLM sample has superior oxidation resistance due to more uniform oxide layers with smaller and well-distributed spinel, whereas the forged sample exhibits greater morphological instability at elevated temperatures.

Fig. 6 shows the phase composition of the SLM and forged samples after oxidation at 1000 °C for 10 h by XRD and EDS in the globular and spinel structures. As shown in Fig. 6a, both samples contain substantial amounts of spinel oxide (like $MnCr_2O_4$), Cr_2O_3 oxide, and the γ matrix, indicating similar oxidation products. Fig. 6b reveals that the globular structure is enriched with Cr (28.56 wt%), whereas the spinel structure has a smaller Cr concentration of 22.62 wt% but a larger Mn concentration of 12.51 wt%, suggesting that the globular structure is predominantly composed of Cr_2O_3, while the spinel structure consists mainly of $MnCr_2O_4$.

After oxidation for 10 h, oxidation is extended to 100 h at 900 °C, 1000 °C and 1100 °C to evaluate the long-term oxidation behavior of SLM-GH5188 and forged-GH5188 (Fig. 7). At 900 °C (Fig. 7a_1-a_2), the SLM-GH5188 superalloy exhibits a relatively uniform oxidized surface with only minor rumpling, indicating a stable and dense spinel structure on the oxide scale. The uniformity suggests that the additive manufacturing process produces a more homogeneous microstructure and a more effective protective oxide layer against oxidation. In contrast, the forged group shows poor oxidative uniformity with large areas of inhomogeneous bulges and the initiation of cracks in these heterogeneous regions (Fig. 7d_1-d_2), indicating that the forging process may introduce microstructural inconsistencies that compromise the

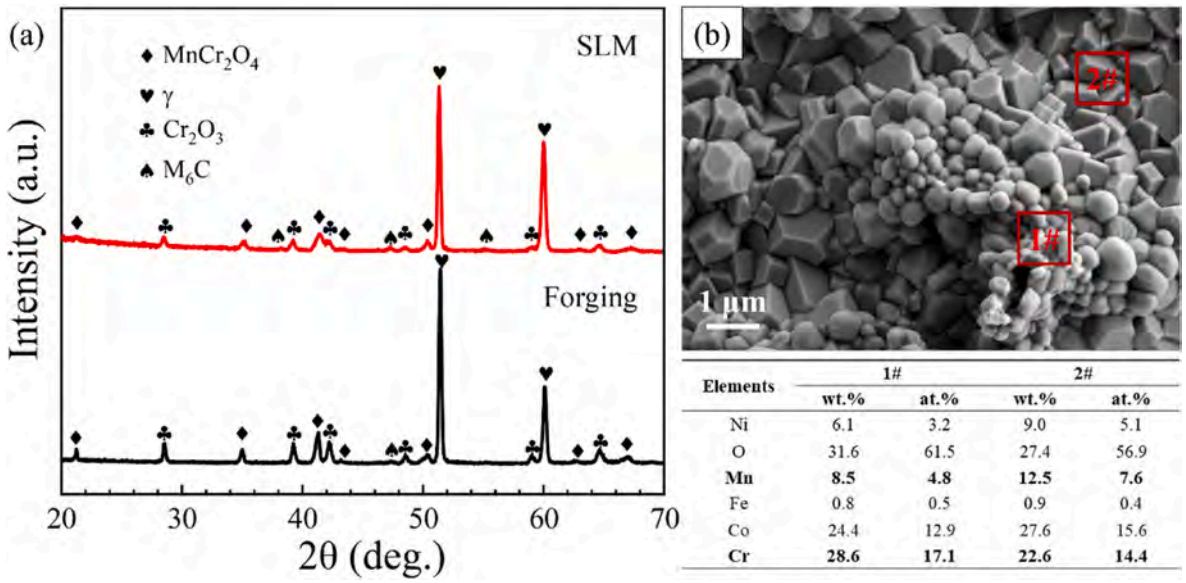

Elements	1#		2#	
	wt.%	at.%	wt.%	at.%
Ni	6.1	3.2	9.0	5.1
O	31.6	61.5	27.4	56.9
Mn	**8.5**	**4.8**	**12.5**	**7.6**
Fe	0.8	0.5	0.9	0.4
Co	24.4	12.9	27.6	15.6
Cr	**28.6**	**17.1**	**22.6**	**14.4**

Fig. 6. (a) XRD patterns of the SLM and forged samples after oxidation for 10 h at 1000 °C; (b) SE and EDS results of the SLM sample after oxidation at 1000 °C for 10 h.

integrity of the oxide scale.

After oxidation at 1000 °C, the SLM-GH5188 surface becomes less flat, as shown by concave and convex regions that reflect heterogeneous oxide growth (Fig. 7b_1-b_2). However, the oxide scale remains more continuous than that on the forged sample. The forged-GH5188 shows a thicker oxide scale with extensive bulging, together with serious cracking and scattered spallation (Fig. 7e_1-e_2). These results show weaker oxidation resistance on the forged-GH5188 at elevated temperature. When the oxidation temperature increases to 1100 °C, the samples show different oxidation trends. The SLM-GH5188 superalloy shows notable bulging and some cracking or collapse of the oxide layer, but without widespread spallation (Fig. 7c_1-c_2). In contrast, the forged-GH5188 superalloy suffers severe spallation and detachment of oxide scale (Fig. 7f_1-f_2), and the remaining oxide scale is heavily fractured, indicative of oxide scale failure.

In recapitulation, after oxidation for 100 h at the three temperatures, SLM-GH5188 consistently maintains a more uniform and well-adherent oxide scale to protect the substrate. On the contrary, forge-GH5188 exhibits premature cracking and spallation. These results indicate the superior long-term oxidation resistance rendered by the homogeneous microstructure and denser oxide layer produced by additive manufacturing.

To investigate the formation of the oxide scale on SLM-GH5188 and forged-GH5188 after long-term oxidation, XRD is conducted after oxidation for 100 h at 900–1100 °C. The oxidation products on both samples are primarily Cr_2O_3 and $MnCr_2O_4$ spinel oxide, while retaining the γ phase (Fig. 8). The M_6C carbide peak at 900 °C diminishes with increasing temperature and disappears above 1000 °C due to dissolution. The $MnCr_2O_4$ spinel phase dominates in SLM-GH5188 due to the denser and more uniform oxide scale (Fig. 8a), but forged-GH5188 shows a stronger γ phase (Fig. 8b), suggesting oxide scale failure and more substrate exposure.

Fig. 9 depicts the cross-sectional morphologies of the oxide scale formed on SLM-GH5188 and forged-GH5188 after oxidation for 100 h at 1000 °C. As shown in Fig. 9a, the oxide scale on SLM-GH5188 is continuous, uniform (thickness of 2.2 ± 0.3 μm), and adherent to the alloy substrate with minor interfacial cavitation. EDS confirms a uniform transition across the interface. In contrast, forged-GH5188 displays an irregular oxide morphology with pronounced undulations ("hill-and-valley" topography) and numerous interfacial particles (red arrows in Fig. 9b). EDS shows that the precipitates are enriched in W. Interfacial cavities (1–6 μm in diameter) are observed almost exclusively at the scale/alloy interface, suggesting that the high-density carbide regions are preferential voids and nucleation sites for accelerated interfacial degradation and compromised scale adhesion.

3.3. Cyclic oxidation at 1000 °C

To assess the dynamic oxidation resistance of the SLM and forged samples, Fig. 10a presents the cyclic oxidation kinetics in air at 1000 °C. The SLM sample shows a significantly lower mass gain than the forged sample (0.545 mg/cm^2), consistent with the mass gain after 100-h isothermal oxidation (0.547 mg/cm^2). However, the forged sample exhibits a mass gain of 1.471 mg/cm^2, approximately 2.7 times higher than that of the SLM sample, and it is significantly higher than the weight gain of 0.741 mg/cm^2 after 100-h isothermal oxidation at 1000 °C, suggesting that the forged sample suffers from severe spallation during cycling. Fig. 10a confirms the extensive spallation of the oxide scale on the forged sample during cycling, revealing collapsed debris at the bottom of the crucible. Fig. 10b shows the parabolic curves of SLM and forged sample according to Fig. 10a, and the parabolic rate constants of the SLM and forged samples are calculated to be 3.07×10^{-3} and 2.76×10^{-2} mg^2/(cm^4 h), respectively, indicating that SLM results in superior oxidation resistance.

Fig. 11 shows the surface morphologies of the SLM and forged samples after 10, 30, and 50 cycles at 1000 °C. The surface morphology of the oxide scale after cyclic oxidation is slightly different from that after isothermal exposure. The oxidized surface on SLM is covered by a compact $MnCr_2O_4$ spinel structure (Fig. 11a_1-c_1). After 50 cycles, only minor cracks are observed, but without spallation (Fig. 11c_2). However, the forged sample has a convex tumor-like structure that breaks and collapses during cycling (Fig. 11d_1-f_2). Hence, the carbide distribution may impact the oxidation resistance.

4. Discussion

The SLM sample shows better oxidation resistance than the forged sample after isothermal and cyclic oxidation. Except for differences in the distribution and size of carbides (Figs. 1–2), the overall microstructure of the samples shows no significant variation. The carbide-related oxidation membrane has a large influence on the oxidation resistance, and in this section, the role of carbide on the formation and

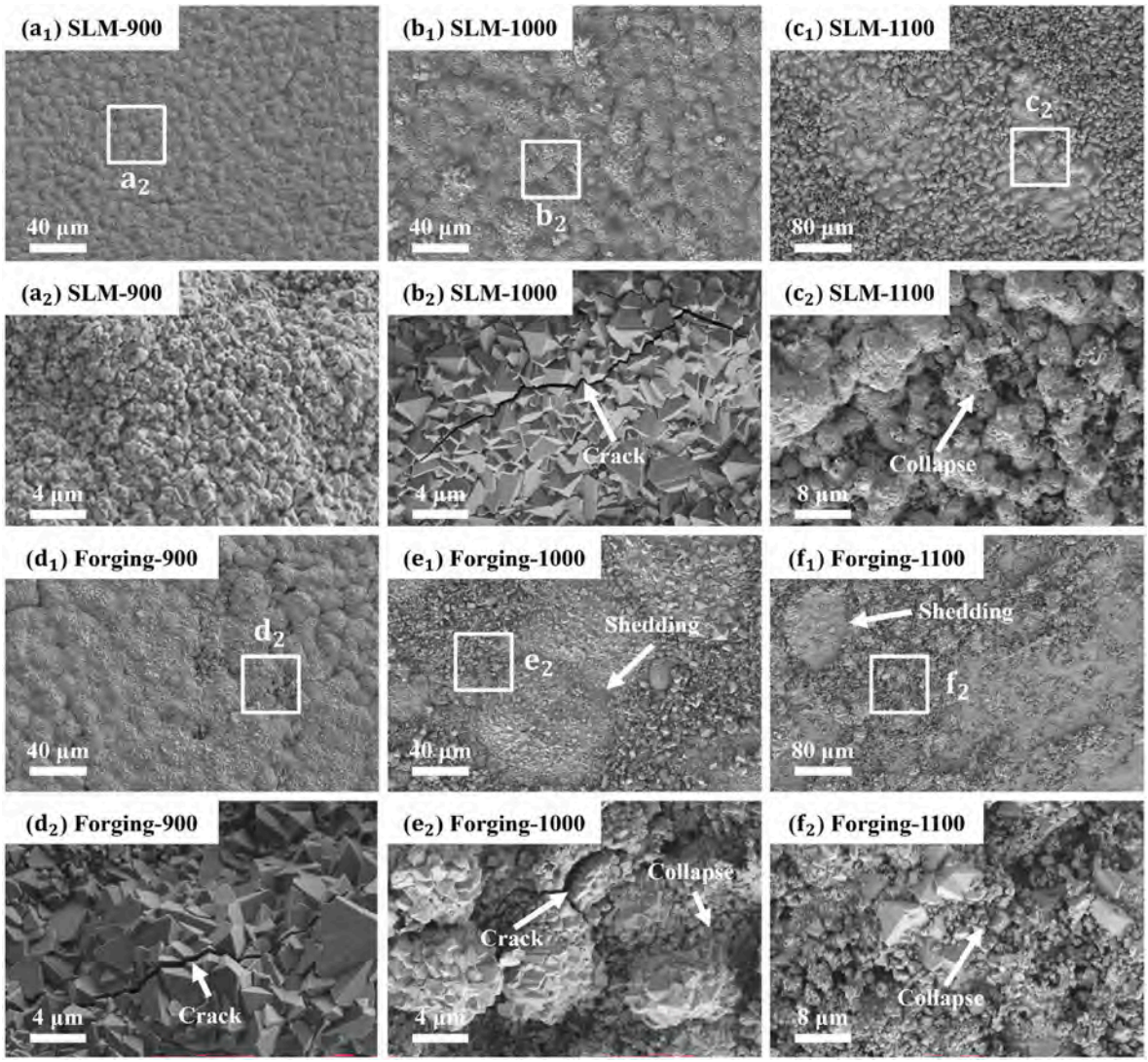

Fig. 7. Surface morphology of the SLM and forged samples after oxidation for 100 h at 900 °C, 1000 °C and 1100 °C: (a_1-a_2, d_1-d_2) Low and high-magnification SE after oxidation for 100 h at 900 °C; (b_1-b_2, e_1-e_2) Low and high-magnification SE images after oxidation for 100 h oxidation at 1000 °C; (c_1-c_2, f_1-f_2) Low and high-magnification SE images after oxidation for 100 h at 1100 °C.

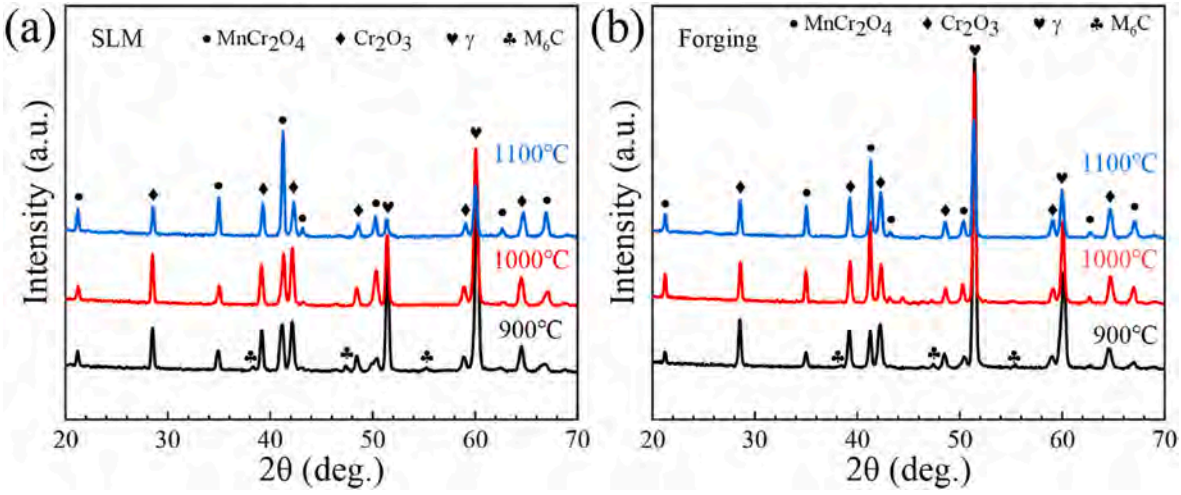

Fig. 8. XRD patterns of (a) SLM-GH5188 and (b) Forged-GH5188 after oxidation at 900 °C, 1000 °C and 1100 °C for 100 h.

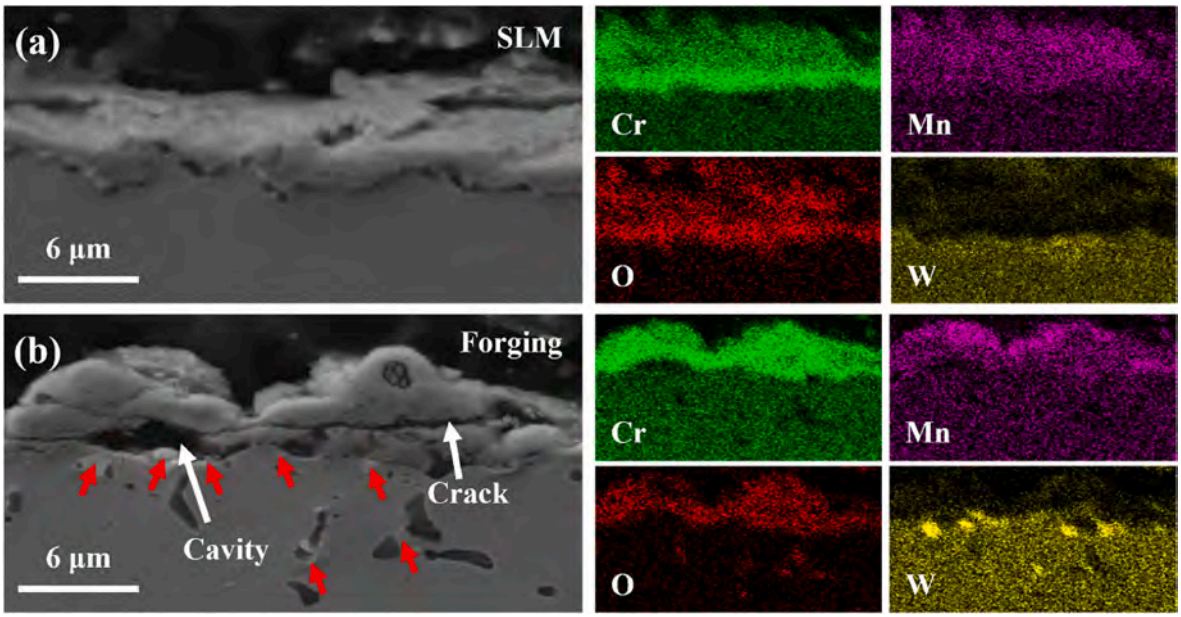

Fig. 9. Cross-sectional morphologies of (a) SLM-GH5188 and (b) Forged-GH5188 after oxidation for 100 h at 1000 °C.

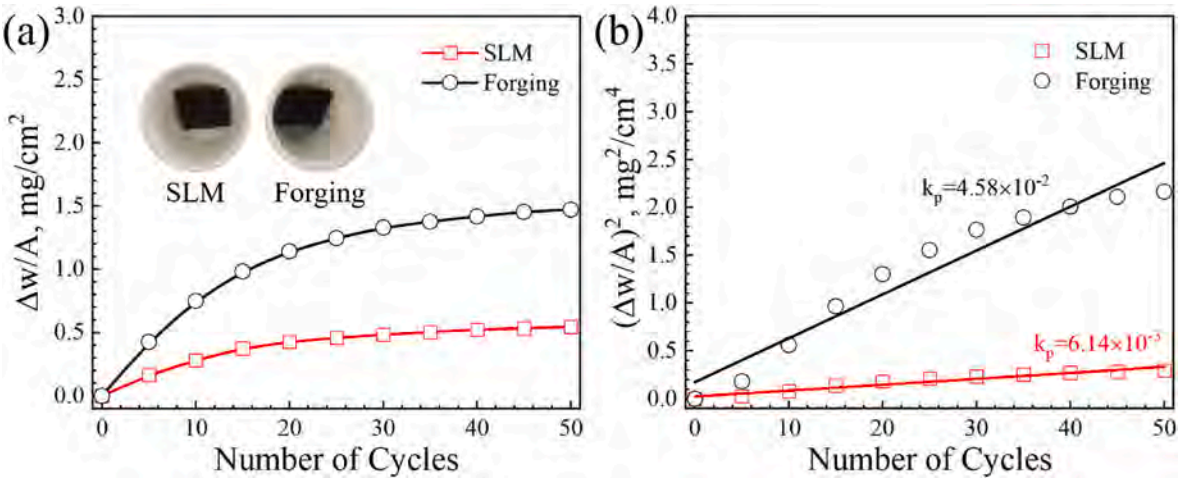

Fig. 10. Mass gains of SLM and forged GH5188 superalloys under cyclic oxidation conditions at 1000 °C for 50 cycles.

failure mechanisms of the oxidation membrane is discussed.

4.1. Formation mechanism of the oxide scale

The primary alloying elements in GH5188 are Co, Cr, W, Ni, Mn, and Fe, which are oxidized to CoO, Cr_2O_3, WO_3, NiO, MnO (or Mn_3O_4), and FeO (or Fe_2O_3, Fe_3O_4). Using the relevant thermodynamic data [35,37], the Gibbs free energy of the oxidation reactions can be calculated (Fig. 12), as shown in Table 1 for the three temperatures. The lowest Gibbs free energy is exhibited by MnO, followed by Cr_2O_3 at temperatures of 900 °C, 1000 °C, and 1100 °C. This indicates that the reactions occur preferentially when Cr and Mn coexist with other alloy elements. Mn tends to participate in oxidation due to the smaller Gibbs free energy. However, the oxidation reaction of Cr is more pronounced because the Mn concentration is only about 1 %. During initial oxidation, the alloying elements in the matrix come into direct contact with oxygen and are oxidized preferentially according to the Gibbs free energy. The different metallic oxides tend to form interfaces, and polymerization generates the spinel structure as shown below:

$$NiO + Cr_2O_3 \rightarrow NiCr_2O_4 \quad (2)$$

$$FeO + Cr_2O_3 \rightarrow FeCr_2O_4 \quad (3)$$

$$MnO + Cr_2O_3 \rightarrow MnCr_2O_4 \quad (4)$$

The spinel oxide can be regarded as a polymer or mixture of two oxides without exchange or transfer of ions and electrons. This means that the Gibbs free energy of the spinel structure is the sum of the Gibbs free energies of the respective oxides. In this system, $MnCr_2O_4$ is the most stable spinel structure due to the smallest Gibbs free energy. Therefore, the oxidation product of the GH5188 superalloy consists of a Cr_2O_3 oxide layer and a $MnCr_2O_4$ spinel structure as demonstrated by XRD and EDS.

While oxide formation is primarily thermodynamic, the oxidation process is governed by concurrent oxidation, reduction reactions, and element migration in the evolving scale. Elements such as Mn can oxidize and react with primary oxides. Although these oxidation stages do not occur in a strictly sequential order, the end-state oxide scale must conform to thermodynamics. Moreover, as the scale thickens, the

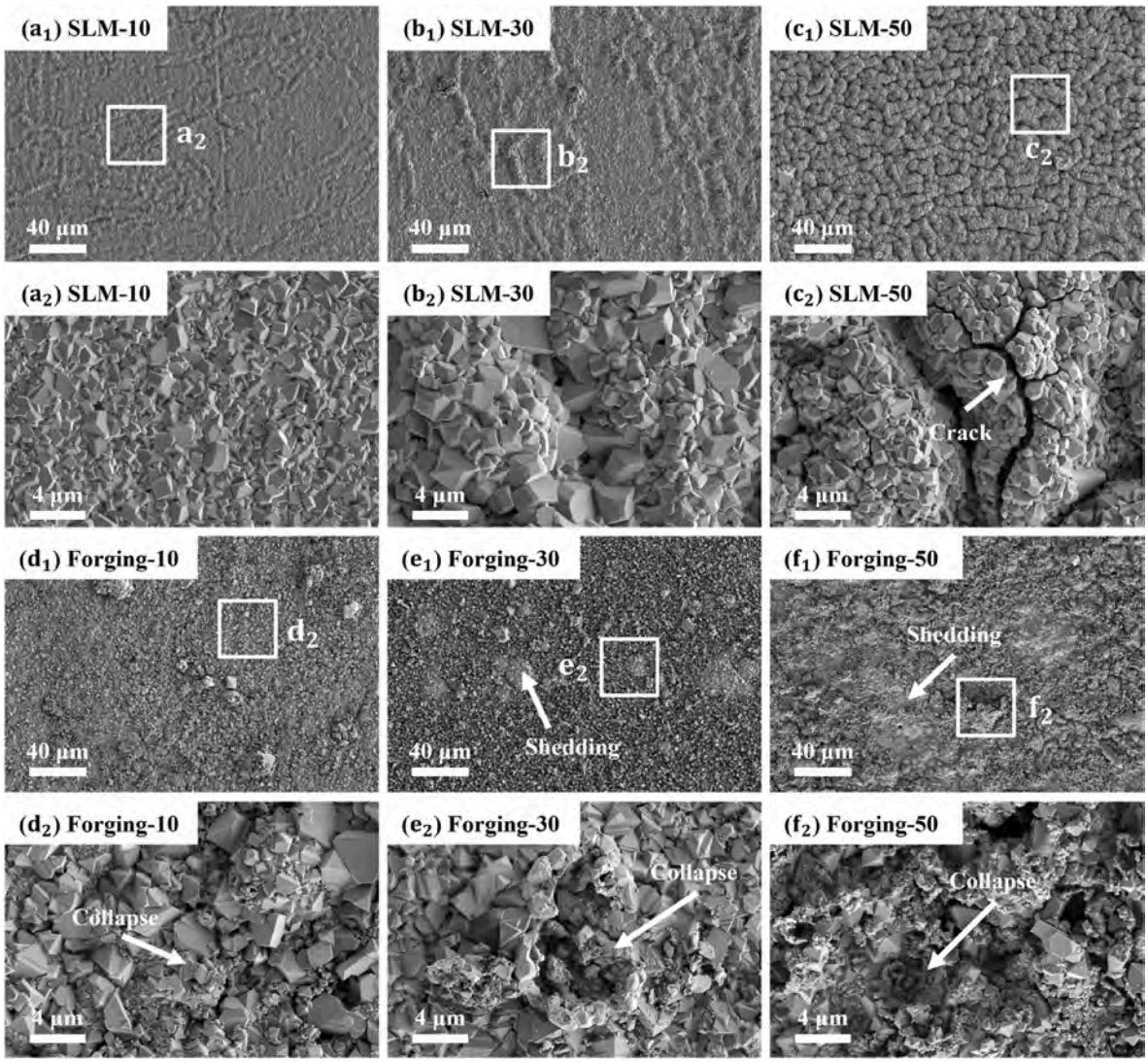

Fig. 11. Surface morphologies of the SLM and forged samples after oxidation for 10, 30, and 50 cycles at 1000 °C: (a_1-a_2, d_1-d_2) Low and high-magnification SE images after 10 cycles; (b_1-b_2, e_1-e_2) Low and high-magnification SE images after 30 cycles; (c_1-c_2, f_1-f_2) Low and high-magnification SE images after 50 cycles.

continuous growth of scale relies increasingly on ionic diffusion, and species with higher diffusivity have greater availability for oxidation at the metal-scale interface. Table 2 lists the diffusion coefficients of the key elements in the principal oxide on GH5188 at 1000 °C [34]. The Cr^{3+} mobility in Cr_2O_3 is quite low, giving rise to superior protection. In contrast, Mn^{2+} diffuses outward more rapidly on account of the small Gibbs free energy of oxidation and preferentially transforms into MnO at the scale-gas interface. MnO then undergoes a solid-state reaction with the underlying Cr_2O_3 to form the mixed spinel-structure of $MnCr_2O_4$. Consequently, the GH5188 superalloy forms a duplex oxide film comprising an inner Cr_2O_3 layer and an outer $MnCr_2O_4$ spinel structure.

Based on the above thermodynamic discussion, an oxide scale formation mechanism is postulated for the GH5188 superalloy, as shown in Fig. 13. In the initial oxidation stage, oxygen dissolves at the alloy surface and reacts preferentially with Cr with the smallest Gibbs free energy to form a continuous Cr_2O_3 layer, alongside minor MnO nucleation. The MnO islands react locally with adjacent Cr_2O_3 to nucleate $MnCr_2O_4$ spinel. As oxidation proceeds, inward diffusion of O^{2-} and outward diffusion of Mn^{2+} continue. Additional Cr_2O_3 grows at the metal/scale interface, while Mn^{2+} reaches the scale/gas boundary to form MnO and convert more Cr_2O_3 into $MnCr_2O_4$. The result is a duplex scale with an inner Cr_2O_3 scale (providing a dense, passivating barrier) and an outer $MnCr_2O_4$ spinel (which lowers the local oxygen partial pressure, further slowing Cr_2O_3 oxidation). After prolonged exposure, Cr_2O_3 volatilizes as CrO_3 gas to thin the protective layer, while the outer spinel mitigates this by reducing the driving force for CrO_3 formation and shedding, eventually enhancing the long-term oxidation resistance.

4.2. Failure mechanism of the oxide scale

While the SLM and forged samples exhibit the same alloy composition and oxide products (inner Cr_2O_3 layer and outer $MnCr_2O_4$ spinel), the oxide scales display markedly different degradation behaviors. Therefore, we will focus on elucidating the failure mechanisms of the oxide scales formed on both the SLM and forged samples and clarifying the reasons for their distinct oxidation resistance in this section.

It is well accepted that oxide spallation occurs when the elastic strain energy stored in the oxide scale exceeds the interfacial fracture energy G_c. This failure criterion is written as [39,40]:

$$\frac{(1-\nu^2)}{2E}\sigma^2 h > G_c \tag{5}$$

where ν and E are the Poisson's ratio and the elastic modulus of the oxide scale. σ and h are residual stress and thickness of the oxide scale, respectively. This criterion highlights that residual stress, scale

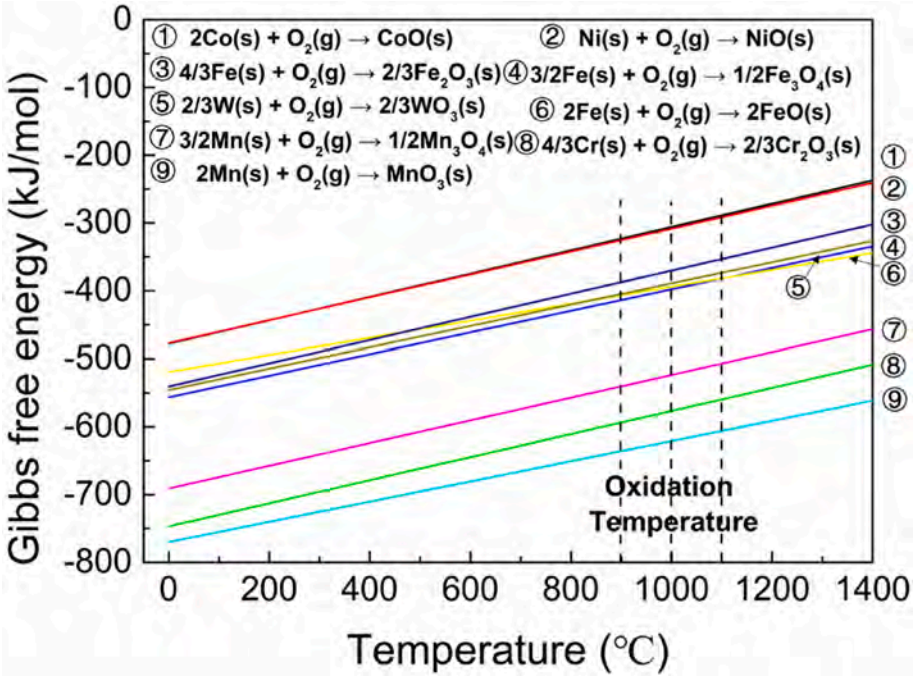

Fig. 12. Relationship between Gibbs free energy of oxidation and temperature.

Table 1
Calculated Gibbs free energies of oxidation at different temperatures.

Oxides	900 °C	1000 °C	1100 °C
CoO	−276.08	−258.88	−241.68
NiO	−279.16	−262.30	−245.44
Cr_2O_3	−547.06	−530.04	−513.01
WO_3	−370.44	−354.59	−338.73
MnO	−595.11	−580.22	−565.33
Mn_3O_4	−494.51	−477.78	−461.04
FeO	−372.47	−359.96	−347.45
Fe_3O_4	−362.02	−346.37	−330.72
Fe_2O_3	−340.79	−323.77	−306.74

Table 2
Diffusion coefficients of ions in metal oxides (1000 °C) [38].

Oxide	Diffusion Coefficient(cm^2/s)
CoO	Co^{2+}:3 × 10^{-9}
NiO	Ni^{2+}:1 × 10^{-11}
Cr_2O_3	Cr^{3+}:1 × 10^{-14}
$CoCr_2O_4$	Co^{2+}:1.7 × 10^{-12}, Cr^{3+}:1.9 × 10^{-12}
$NiCr_2O_4$	Ni^{2+}:1.4 × 10^{-13}, Cr^{3+}:2.8 × 10^{-13}
MnO	Mn^{2+}:1 × 10^{-10}

thickness, and interfacial fracture energy are the three critical factors governing spallation resistance.

The residual stress in oxide scales at room temperature consists of two components, the thermal mismatch stress (σ_T) and growth stress (σ_g) [41]. The thermal mismatch stress (σ_T) originates from the difference in coefficient of thermal expansion (CTE) between the substrate alloy and oxide scale and the growth stress (σ_g) is generated by the lateral growth of oxide scale. Since the alloy composition and oxide products are similar for both SLM and forged sample, σ_T and σ_g can be regarded as comparable. However, the forged samples exhibit a much thicker oxide scale than the SLM samples due to their higher oxidation rate. This difference is closely related to grain size: the fine grains of the SLM samples (500 nm-1 μm) provide a higher grain boundary density that promotes uniform nucleation and rapid healing of the initial oxide, forming a dense and adherent scale. In contrast, the coarse grains of the forged samples (~10 μm) reduce nucleation sites and lead to a more porous, non-uniform scale. Consequently, the elastic strain energy of the thicker oxide scale on the forged samples is much higher than that of the SLM samples.

The interfacial fracture energy G_c is governed by impurity segregation and interfacial imperfections [42,43]. As shown in Fig. 9, numerous interfacial cavities are observed preferentially nucleating around the W-rich carbides in the forged samples, whereas no such cavities are detected in the SLM samples. These cavities originate from the volatilization of oxides such as CrO_3 and WO_3 at elevated temperatures, which increases interfacial porosity and significantly reduce the interfacial fracture energy. Although a dense Cr_2O_3 oxide film inhibits continuous oxidation of the substrate [44], the stability of Cr_2O_3 decreases at elevated temperatures due to the possible formation of volatile Cr^{6+} species via:

$$4Cr_2O_3(s) + 3O_2(g) \rightarrow 4CrO_3(g). \quad (6)$$

This solid-gas transition is thermodynamically feasible starting from 200 to 300 °C, but only a limited amount of CrO_3 forms at intermediate temperatures such as 600 °C due to kinetic constraints [45]. However, it is reported that the formation of Cr^{6+} species generally occurs above 900 °C, as both the thermodynamic driving force ($\Delta G < 0$) and kinetic factors (e.g. activation energy) become sufficiently favorable only at these elevated temperatures. Therefore, the degradation of protective Cr_2O_3 scales by CrO_3 volatilization becomes critical under high-temperature conditions. The formation of epitaxial $MnCr_2O_4$ spinel scale can reduce the volatilization rate by increasing the activation energy required for oxidation of Cr^{3+} to Cr^{6+} [46].

The coarse W-rich M_6C carbides in the forged GH5188 alloy further amplify degradation through a synergistic mechanism of elemental depletion and defect generation. Their interfaces with the matrix serve as rapid diffusion channels for W and Cr, promoting selective oxidation and localized thickening of the oxide scale (Fig. 5d–f and **11d**) [47]. Moreover, decomposition of W-rich carbides followed by oxidation produces volatile WO_3 at the carbide/oxide interface, generating interfacial pores. When the volume fraction of pores exceeds a critical level, the beneficial effect of the $MnCr_2O_4$ spinel is diminished, leading to scale

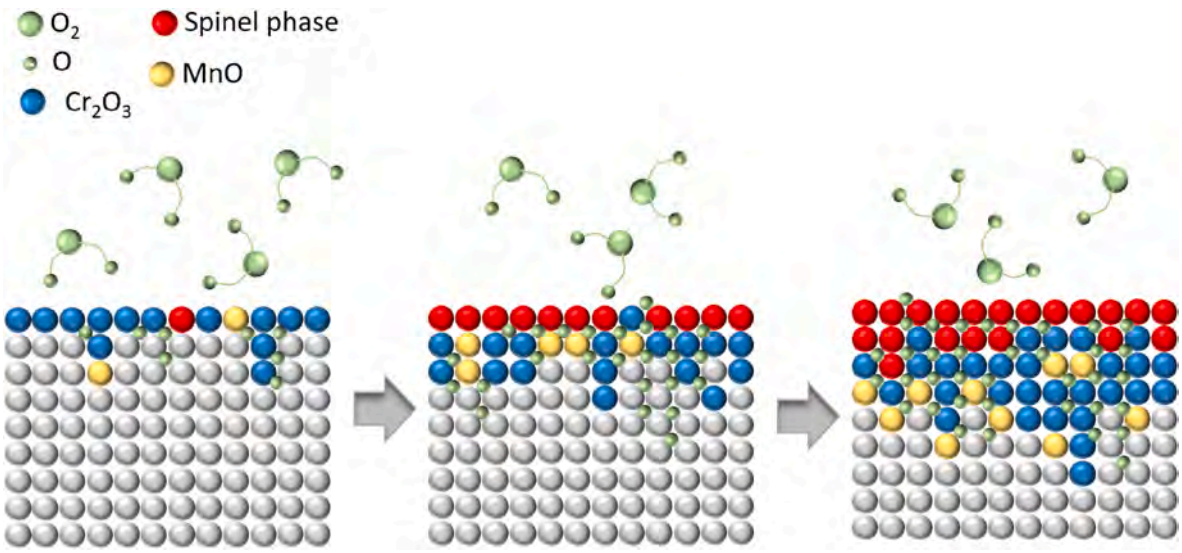

Fig. 13. Schematic of the oxidation mechanism of the GH5188 alloy.

delamination [48,49]. During long-term oxidation, continued volatilization of WO_3 and CrO_3 enhances pore connectivity, reduces the effective diffusion path for ions, and triggers crack initiation in the spinel layer.

Fig. 14 shows the failure mechanism of the oxide scale formed on the forged GH5188 superalloy based on the correlation between the microstructural evolution and oxidation kinetics. In the initial stage, volatilization of CrO_3 (originating from the Cr_2O_3) and WO_3 (formed by the oxidation of decomposed W-rich M_6C carbides) leads to the formation of interfacial cavities (Fig. 14b). Prolonged thermal exposure increases the internal gas pressure [50] and produces thermal mismatch and growth stress that amplifies surface roughening of the oxide scale (Fig. 14c). Once the stored elastic strain energy surpasses the interfacial fracture energy, brittle spallation of the $MnCr_2O_4$ spinel scale occurs, exposing the substrate to rapid oxidation (Fig. 14d). Newly formed cracks act as fast oxygen ingress channels, establishing a self-sustaining "cavity–crack–oxidation" degradation cycle.

In comparison, the refined microstructure of the SLM-GH5188 alloy disrupts this cycle. Fine cellular sub-grains (500 nm-1 μm) confine M_6C carbides as nanoscale precipitates (80 ± 20 nm) at grain-boundary triple junctions, increasing the activation energy for carbide decomposition and suppressing WO_3 volatilization (Fig. 15). As a result, SLM-GH5188 maintains a uniform and adherent oxide scale, leading to superior oxidation resistance at elevated temperatures. This study correlates thermodynamic predictions with oxidation kinetics and detailed microstructural observations, providing fundamental insights into the mechanisms governing oxidation resistance in additively manufactured GH5188 superalloys.

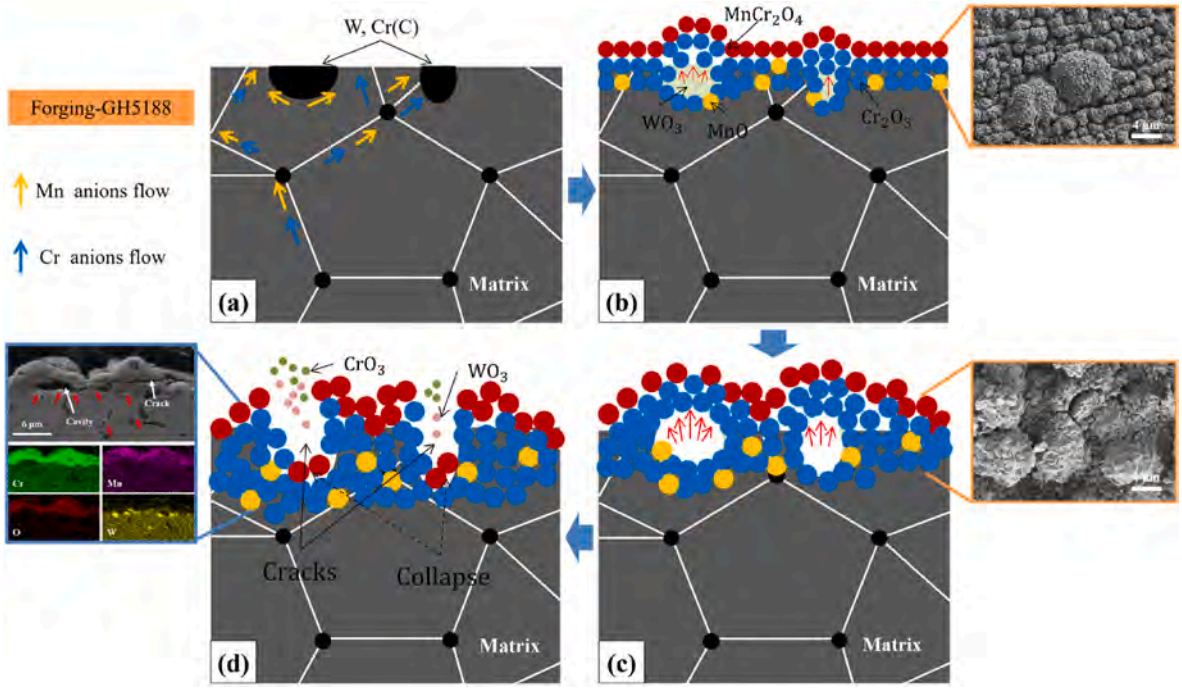

Fig. 14. Schematic illustrating the oxidation membrane failure mechanism of forged-GH5188 sample.

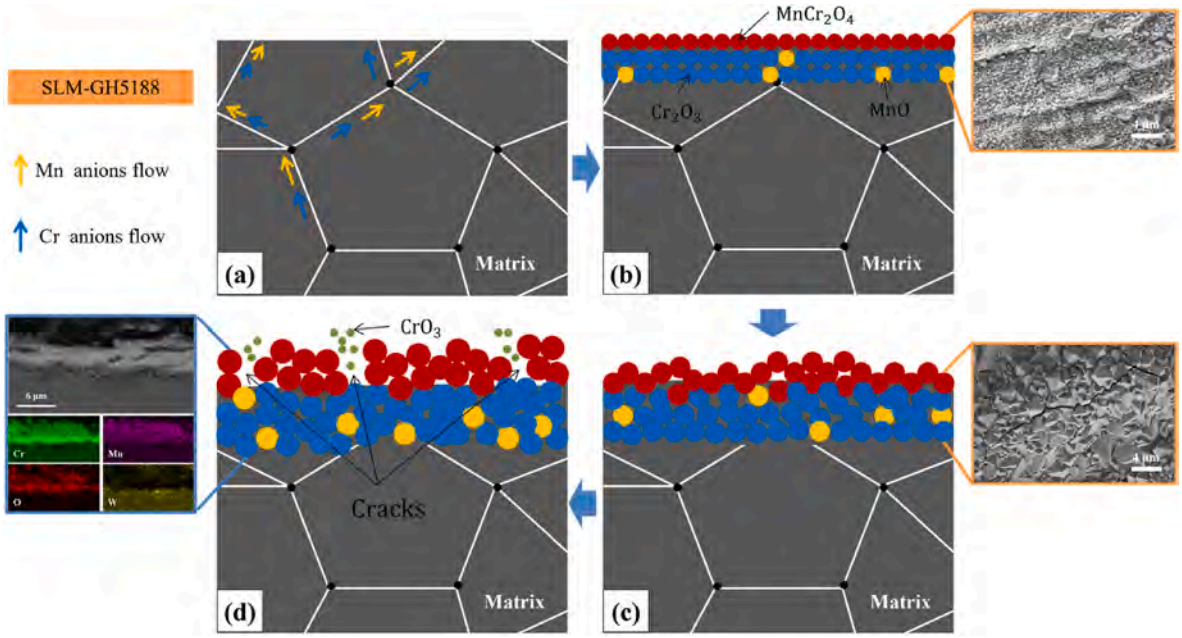

Fig. 15. Schematic illustrating the oxidation membrane failure mechanisms of the SLM GH5188 samples.

5. Conclusion

The high-temperature oxidation behavior of GH5188 Co-based superalloy fabricated by SLM and forging is investigated. The SLM-processed samples have a hierarchical microstructure consisting of fibrous and cell-shaped grains with a 100 nm to micrometer scale, while the forged samples show equiaxed grains with sizes of ~10 μm. The fine uniform carbide (~80 nm) is pinned to the tripartite grain boundaries of the SLM samples, whereas coarse W-rich M_6C carbide (~5 μm) is embedded in the grain boundaries of the forged samples. The weight gains of the SLM samples are only 69 % and 75 % of those of the forged sample after 200-h isothermal oxidation at 1000 °C and 1100 °C. After cyclic oxidation at 1000 °C, the SLM sample shows a mass gain of only 0.545 mg/cm^2 after 50 cycles, while the forged sample shows a mass increase of up to 1.471 mg/cm^2. The coarse W-rich M_6C carbide (~5 μm) in the forged sample reduces the bond strength of the oxide scale to the substrate and produces WO_3 gas during high-temperature oxidation, leading to the failure of the oxide scale. The hierarchical SLM sample with fine and uniform M_6C carbide reduces the diffusion rate of the alloying elements to form a stable oxide scale and improve the adhesion between the oxide scale and alloy substrate, ultimately enhancing the high-temperature oxidation resistance of the GH5188 superalloy.

CRediT authorship contribution statement

Chao Yang: Writing – original draft, Investigation. **Xue Chen:** Writing – original draft, Formal analysis, Data curation. **Yusheng Tian:** Visualization, Formal analysis. **Yifeng Tang:** Methodology, Formal analysis. **Shiping Cai:** Visualization, Formal analysis. **Wei Wei:** Supervision, Resources, Conceptualization. **Qianli Huang:** Validation, Investigation. **Hang Guo:** Visualization, Methodology. **Aihui Huang:** Writing – review & editing, Project administration. **Paul K. Chu:** Writing – review & editing.

Declaration of competing interest

The authors declare the following financial interests which may be considered as potential competing interests: Hang Guo are currently employed by the Yan'an Yanhong Intelligent Manufacturing Technology Development Co., Ltd.

Acknowledgements

This work was supported by the National Natural Science Foundation of China (Nos. 51931003 and 52401101), and China Postdoctoral Science Foundation (Nos. 2024T170557, 2023M742224, and 2020M680223), Postdoctoral Fellowship Program of CPSF under Grant Number GZC20231545, Shanghai Post-doctoral Excellence Program (No. 2023440), as well as City University of Hong Kong Donation Research Grants (DON-RMG Nos. 9229021 and 9220061).

References

[1] C.T. Sims, N.S. Stoloff, W.C. Hagel, I.I. Superalloys, High Temperature Materials for Aerospace and Industrial Power, Eds., John Wiley and Sons, New York, 1987.
[2] J. Sato, T. Omori, K. Oikawa, I. Ohnuma, R. Kainuma, K. Ishida, Cobalt-base high-temperature alloys, Science 312 (2006) 90–91.
[3] X.S. Zhang, Y.J. Chen, J.L. Hu, Recent advances in the development of aerospace materials, Prog. Aero. Sci. 97 (2018) 22–34.
[4] C. Wang, F. Xue, X. Li, Y. Chen, Q. Deng, A. Li, H. Long, S. Mao, W. Li, L. Yang, Q. Feng, X. Han, Multidimensional microscopic investigation of oxidation-induced hollow cavities in a Co–Al–W–Ti–Ta alloy nanotip by electron tomography, J. Alloys Compd. 848 (2020) 156243.
[5] E.M. Lehockey, G. Palumbo, P. Lin, Improving the weldability and service performance of nickel-and iron-based superalloys by grain boundary engineering, Metall. Mater. Trans. A 29 (1998) 3069–3079.
[6] S. Kamal, R. Jayaganthan, S. Prakash, S. Kumar, Hot corrosion behavior of detonation gun sprayed Cr_3C_2-NiCr coatings on Ni and Fe-based superalloys in Na_2SO_4-60% V_2O_5 environment at 900 ∘C, J. Alloys Compd. 463 (2008) 358–372.
[7] H. Singh, D. Puri, S. Prakash, Some studies on hot corrosion performance of plasma sprayed coatings on a Fe-based superalloy, Surf. Coat. Technol. 192 (2005) 27–38.
[8] N. Birks, G.H. Meier, F.S. Pettit, Introduction to the High Temperature Oxidation of Metals, Cambridge university press, 2006.
[9] R. Darolia, Development of strong, oxidation and corrosion resistant nickel-based superalloys: critical review of challenges, progress and prospects, Int. Mater. Rev. 64 (2019) 355–380.
[10] C. Yang, T. Ying, A.H. Huang, J. Huang, P.H. Chen, P.K. Chu, X.Q. Zeng, Enhancing the corrosion resistance of MAO coatings on LY12 alloy by in situ co-doping with zinc phosphate and cerium phosphate, Corros. Commun. 17 (2025) 35–43.
[11] M. Weiser, S. Virtanen, Influence of W content on the oxidation behaviour of ternary γ'-Strengthened Co-Based model alloys between 800 and 900 °C, Oxid. Metals 92 (2019) 541–560.
[12] Y. Chen, F. Xue, C. Wang, X. Li, Q. Deng, X. Yang, H. Long, W. Li, L. Yang, A. Li, Effect of Cr on the microstructure and oxidation properties of Co-Al-W superalloys studied by in situ environmental TEM, Corros. Sci. 161 (2019) 108179.
[13] Haynes Alloy 188, Report-Haynes International, Inc., Kokomo, TN, 1991.
[14] M.D. Rowe, V.R. Ishwar, D.L. Klarstrom, Properties, weldability, and applications of modern wrought heat-resistant alloys for aerospace and power generation industries, Trans. ASME 128 (2006) 354–361.

[15] C. Guo, S. Li, S. Shi, X. Li, X. Hu, Q. Zhu, R.M. Ward, Effect of processing parameters on surface roughness, porosity and cracking of as-built IN738LC parts fabricated by laser powder bed fusion, J. Mater. Process. Technol. 285 (2020) 116788.
[16] Q. Guo, C. Zhao, L.I. Escano, Z. Young, L. Xiong, K. Fezzaa, W. Everhart, B. Brown, T. Sun, L. Chen, Transient dynamics of powder spattering in laser powder bed fusion additive manufacturing process revealed by in-situ high-speed high-energy x-ray imaging, Acta Mater. 151 (2018) 169–180.
[17] Michele Calandri, Diego Manfredi, Flaviana Calignano, Elisa Paola Ambrosio, Sara Biamino, Rocco Lupoi, Daniele Ugues, Solution treatment study of inconel 718 produced by SLM additive technique in view of the oxidation resistance, Adv. Eng. Mater. 20 (2018) 1800351.
[18] M. Romedenne, R. Pillai, M. Kirka, S. Dryepondt, High temperature air oxidation behavior of hastelloy X processed by Electron Beam Melting (EBM) and Selective Laser Melting (SLM), Corros. Sci. 171 (2020) 108647.
[19] Q. Chen, G. Guillemot, C. Gandin, et al., Three-dimensional finite element thermomechanical modeling of additive manufacturing by selective laser melting for ceramic materials, Addit. Manuf. 16 (2017) 124–137.
[20] A.V. Sotov, A.V. Agapovichev, V.G. Smelov, et al., Investigation of the IN-738 superalloy microstructure and mechanical properties for the manufacturing of gas turbine engine nozzle guide vane by selective laser melting, Int. J. Adv. Manuf. Technol. 107 (5–6) (2020) 2525–2535.
[21] M. Huguet, G. Boissonnet, G. Lotte, J. Cormier, P. Villechaise, G. Bonnet, F. Pedraza, High temperature oxidation of additively manufactured rene 65, Corros. Sci. 220 (2023) 111273.
[22] W. Wei, J.C. Xiao, C.F. Wang, Q. Cheng, F.J. Guo, Q. He, M.S. Wang, S.Z. Jiang, C. X. Huang, Hierarchical microstructure and enhanced mechanical properties of SLM-fabricated GH5188 Co-superalloy, Mater. Sci. Eng., A 831 (2022) 142276.
[23] S. Parizia, G. Marchese, M. Rashidi, M. Lorusso, E. Hryha, D. Manfredi, S. Biamino, Effect of heat treatment on microstructure and oxidation properties of Inconel 625 processed by LPBF, J. Alloys Compd. 846 (2020) 156418.
[24] A. Chyrkin, K.O. Gunduz, I. Fedorova, M. Sattari, A. Visibile, M. Halvarsson, J. Froitzheim, K. Stiller, High-temperature oxidation behavior of additively manufactured IN625: effect of microstructure and grain size, Corros. Sci. 205 (2022) 110382.
[25] E.R. Lewis, M.P. Taylor, B. Attard, N. Cruchley, A.P.C. Morrison, M.M. Attallah, S. Cruchley, Microstructural characterisation and high-temperature oxidation of laser powder bed fusion processed Inconel 625, Mater. Lett. 311 (2022) 131582.
[26] T. Sanviemvongsak, D. Monceau, C. Desgranges, B. Macquaire, Intergranular oxidation of Ni-base alloy 718 with a focus on additive manufacturing, Corros. Sci. 170 (2020) 108684.
[27] X. Liu, R. Hu, H. Zou, M. Zhou, Z. Gao, K. Zhang, J. Zheng, J. Bai, R. Ma, High-temperature oxidation behavior of a novel γ′-strengthened superalloy manufactured by laser-beam powder bed fusion: effect of post-heat treatment, Corros. Sci. 239 (2024) 112384.
[28] C. Guo, Y. Li, Y. Li, G. Li, X. Lu, Z. Li, X. Chen, X. Li, L. Zhou, Q. Zhu, J. Lu, High-temperature oxidation behaviour of a Co-based superalloy fabricated through laser powder bed fusion, Corros. Sci. 227 (2024) 111703.
[29] Y. Wu, B. Sun, B. Chen, P. Chen, T. Yan, X. Zhang, C. Huang, W. Liu, Cracking mechanism of GH5188 alloy during laser powder bed fusion additive manufacturing, Mater. Char. 207 (2024) 113548.
[30] A. Keshavarzkermani, M. Sadowski, L. Ladani, Direct metal laser melting of Inconel 718: process impact on grain formation and orientation, J. Alloys Compd. 736 (2018) 297–305.
[31] N.B. Pilling, R.E. Bedworth, The oxidation of metals at high temperature, J. Inst. Met. 29 (1923) 529.
[32] S. Sun, K. Hagihara, T. Nakano, Effect of scanning strategy on texture formation in Ni-25 at.% Mo alloys fabricated by selective laser melting, Mater. Des. 140 (2018) 307–316.
[33] B. Han, et al., Additively manufactured high strength and ductility CrCoNi medium entropy alloy with hierarchical microstructure, Mater. Sci. Eng., A 820 (2021) 141545.
[34] A. Bauer, S. Neumeier, F. Pyczakc, M. Goken, Microstructure and creep strength of different γ/γ'-strengthened Co-base superalloy variants, Scr. Mater. 63 (2010) 1197–1200.
[35] D. Wang, C. Song, Y. Yang, Y. Bai, Investigation of crystal growth mechanism during selective laser melting and mechanical property characterization of 316L stainless steel parts, Mater. Des. 100 (2016) 291–299.
[36] L.E. Murr, S.M. Gaytan, D.A. Ramirez, E. Martinez, J. Hernandez, K.N. Amato, P. W. Shindo, F.R. Medina, R.B. Wicker, Metal fabrication by additive manufacturing using laser and electron beam melting technologies, J. Mater. Sci. Technol. 28 (1) (2012) 1–14.
[37] D. Young. High Temperature Oxidation and Corrosion of Metals, Elsevier, Amsterdam, 2016.
[38] I. Barin, G. Platzki, Thermochemical Data of Pure Substances, Weinheim, Newyork, 1995.
[39] A. Huang, L. Li, X. Liu, H. Zhang, M. Li, X. Zhang, J. Lu, X. Zhao, Superior oxidation resistance of a Y-Hf co-doped $Al_{18}Co_{30}Cr_{10}Fe_{10}Ni_{32}$ eutectic high-entropy alloy at 1100-1300 °C, J. Alloys Compd. 992 (2024) 174597.
[40] L. Qiu, F. Yang, W. Zhang, X. Zhao, P. Xiao, Effect of Al content on the lifetime of thermally grown oxide formed on Ni–Al alloys after isothermal oxidation, Corros. Sci. 89 (2014) 13–20.
[41] I.G. Wright, R.B. Dooley, A review of the oxidation behaviour of structural alloys in steam, Int. Mater. Rev. 55 (2010) 129–167.
[42] A. Huang, C. Yang, X. Liu, H. Zhang, F. Guo, B. Qian, J. Lu, X. Zhao, P.K. Chu, Oxidation behavior and failure mechanism of NiCoCrAl eutectic multi-principal element alloys co-doped with Y and Hf at 1100 °C and 1200 °C, Corros. Sci. (2025) 112944.
[43] J. Lu, Y. Chen, C. Zhao, H. Zhang, L. Luo, B. Xu, X. Zhao, F. Guo, P. Xiao, Significantly improving the oxidation and spallation resistance of a MCrAlY alloy by controlling the distribution of yttrium, Corros. Sci. 153 (2019) 178–190.
[44] L.I. Leont'ev, K.V. Grigorovich, M.V. Kostina, The development of new metallurgical materials and technologies. Part 1, Steel Translat. 46 (2016) 6–15.
[45] D. Wang, J. Zhang, L.H. Lou, Formation and stability of nano-scaled $M_{23}C_6$ carbide in a directionally solidified Ni-base superalloy, Mater. Char. 60 (12) (2009) 1517–1521.
[46] T. Sanviemvongsak, D. Monceau, B. Macquaire, High temperature oxidation of IN 718 manufactured by laser beam melting and electron beam melting: effect of surface topography, Corros. Sci. 141 (2018) 127–145.
[47] X. Ledoux, S. Mathieu, M. Vilasi, et al., Oxide growth characterization during short-time oxidation of a commercially available chromia-forming alloy (HR-120) in air at 1,050 °C, Oxid. Metals 80 (1–2) (2013) 25–35.
[48] A. Huang, Y. Tian, Y. Tang, G. Zhu, S. Xia, X. Zhao, P.K. Chu, C. Yang, X. Zeng, Temperature-dependent oxidation behavior of Y-Hf co-doped and Co-free Al16Cr20Fe20Ni44 eutectic multi-principal elements alloy at 1100–1300 °C, Corros. Sci. 255 (2025) 113116.
[49] T. Perez, L. Latu-Romain, R. Podor, et al., In situ oxide growth characterization of Mn-Containing Ni-25Cr (wt. %) model alloys at 1050°C, Oxid. Metals 89 (5–6) (2018) 781–795.
[50] H.E. Evans, Stress effects in high temperature oxidation of metals, Int. Mater. Rev. 40 (1) (1995) 1–20.